Continuous resistance welding of thermoplastic composites: modelling of heat generation and heat transfer

Huajie Shi[1], Irene Fernandez Villegas[1]*, Marc-André Octeau[2], Harald E.N. Bersee[1], Ali Yousefpour[2]

[1]Structural Integrity & Composites, Faculty of Aerospace Engineering, Delft University of Technology, Kluyverweg 1, 2629 HS Delft, the Netherlands

[2]Aerospace Portfolio, National Research Council Canada, 5145 Decelles Avenue, Montréal, Québec, H3T 2B2, Canada

* Corresponding author: Irene Fernandez Villegas (I.FernandezVillegas@tudelft.nl)

Tel: +31(0)15 278 9745; Fax: +31(0)15 278 1151

Email of other authors: H.Shi (H.Shi@tudelft.nl); Marc-André Octeau (marc-andre.octeau@nrc.ca); Harald E. N. Bersee (H.E.N.Bersee@tudelft.nl); Ali Yousefpour (Ali.Yousefpour@cnrc-nrc.gc.ca)

Abstract

A process model composed of electrical and heat transfer models was developed to simulate continuous resistance welding of thermoplastic composites. Glass fabric reinforced polyphenylenesulfide welded in a lap-shear configuration with a stainless steel mesh as the heating element was considered for modelling and experimental validation of the numerical results. The welding temperatures predicted by the model showed good agreement with the experimental results. Welding input power and welding speed were found to be the two most important parameters influencing the welding temperature. The contact quality between the electrical connectors and the heating element was found to influence the distribution of the welding temperature transverse to the welding direction. Moreover, the size of the electrical connectors was found to influence the achievable welding speed and required power input for a certain welding temperature.

Keywords

A. Polymer-matrix composites (PMCs); A. Thermoplastic resin; E. Joints/joining

1. Introduction

Compared with thermoset composites, thermoplastic composite materials have several advantages such as intrinsically higher toughness, better environmental resistance, and sustainability [1, 2]. Furthermore, thermoplastic composites offer the possibility of cost-effective manufacturing and assembling through

thermoforming and welding [3, 4]. Resistance welding has been identified as one of the most promising welding techniques for joining thermoplastic composites [5-7]. It features short cycle times and potentially inexpensive equipment requirements. Static resistance welding (RW), which entails one-shot welding of the entire welding area, has been widely used for welding of coupons or small- to medium-size components [8-12]. However, for larger applications, RW has some drawbacks such as significant non-uniform temperature distribution at the weld interface, high force needs to be applied on the adherends, difficulties to maintain uniform pressure at the weld area and a high power demand [5, 11]. Sequential resistance welding (SRW) was introduced to address these issues [13, 14]. SRW relies on the use of multiple heating elements for a multiple-step welding process, and it successfully overcomes some of the drawbacks of RW for the welding of large parts. However, it introduces some difficulties derived from the handling of multiple heating elements [13, 14]. More recently, a continuous resistance welding (CRW) process has been developed [15]. CRW simplifies the welding process as compared to SRW by using a single-piece heating element and a rack of multiple adjacent copper block connectors, which are parallel to the welding direction and located on both sides of the welding overlap, as depicted in Figure 1. Two copper wheels, connected to the power supply unit, are rolled along the block connectors to generate heat and to create a local molten zone, which moves along the entire welding overlap. Compared to RW, both SRW and CRW introduce new parameters in the welding process and, hence increased complexity but they make it possible to weld larger areas with minimum force and power requirements.

As shown in literature, process modelling combined with experimental validation allows for a better understanding of welding processes and the influence of critical parameters [16-21]. Until now, substantial effort has been devoted to the development of process models for the RW process but no simulation model is available in the open literature for the SRW or the CRW processes. The bigger complexity of both SRW and CRW however justifies the development of dedicated models to improve our understanding of the processes and to fully profit from their advantages.

The objective of this study is to investigate the thermal behaviour of thermoplastic composites during the CRW process as well as the influence of the key welding parameters on the welding temperature. To this aim, a dedicated 3D process model was developed consisting of an electrical and a heat transfer model. The electrical model provided the distribution of resistive heat generation in the heating element. The heat transfer model used this distribution to simulate the welding temperature. Likewise, a parametric study

was conducted to understand the effects of electrical clamping pressure, input power, welding speed and size of the electrical connectors on the welding temperature.

2. Experimental

2.1. Materials

The thermoplastic composite material used in this study was 8HS woven E-glass fabric reinforced polyphenylenesulfide (GF/PPS). GF/PPS laminates were manufactured out of eight layers of CETEX® GF/PPS prepreg, supplied by Ten Cate Advanced Composites, The Netherlands, with a $[(0°/90°)]_{4S}$ stacking sequence. The stack of prepreg was consolidated in a hot platen press at 320 °C and under 1.0 MPa pressure for 15 minutes to obtain 1.9 mm-thick laminates with 50% resin volume fraction.

A plain woven AISI 304L stainless steel mesh, with a wire diameter of 0.04 mm, a gap of 0.09 mm between consecutive wires, and 0.08 mm thickness, was used as the heating element. Stainless steel mesh sheets, dimensions 254 mm × 60 mm, were used at the welding interface. In order to fill the gaps of the mesh and to provide a resin rich area at the welding interface, one layer of 90 µm-thick neat PPS film was placed between the mesh and each adherend prior to welding.

2.2. Continuous resistance welding

The continuous resistance welding setup developed by the National Research Centre of Canada was used in this study [15]. As shown in Figures 2 and 3, the welding setup consisted of a power supply, a pneumatic system for welding compaction, a pneumatic system for electrical clamping, a linear actuator system, block and wheel connectors and thermal insulators. An XDC 60-200 digital DC power supply, I_{max} = 200 A and U_{max} = 60 V, was used to provide the welding input power. For thermal insulation, 12.7 mm-thick GPO3 fibre glass sheets, provided by K-Mac-Plastics (USA), were placed below and above the adherends. As shown in Figure 3, single-lapped GF/PPS joints were welded with an overlapping area of 254 mm × 25.4 mm. Two racks of electrical connectors, each one consisting of twenty copper blocks were used to introduce the electrical power into the heating element. Each copper block was 16 mm long, 12.7 mm wide and 6 mm high. One rack of these block connectors was placed on top of one of the adherends and the other one was placed underneath the other adherend to weld a single lap joint (see Figure 3). A 1 mm-long clamping distance [12] was left between the edges of the overlap and the block connectors. A 55 N electrical clamping force, which equals to approximately 0.30 MPa clamping pressure, was applied to the block connectors through two copper wheel connectors connected to the power supply unit and to a pneumatic cylinder (see Figure 2). Likewise, 500 N welding compaction

force was applied to the welding stack through a series of adjacent compaction rollers connected to a second pneumatic cylinder. During the welding process, the platform on which the adherends, heating element, insulator blocks and block connectors were located was horizontally displaced by a high torque step motor. The connector wheels and the compaction rollers, the support of which remained stationary, were consequently forced to roll at the same constant speed on top of the block connectors and the uppermost insulation block, respectively. An in-house developed LabView program was used to control and record the main welding parameters, namely input power and welding speed, as well as thermocouple readings during the welding process. The welding process was carried out at a constant welding voltage of 4.3 V.

3. Modelling

A flowchart for the CRW process model is presented in Figure 4. This process model is divided into an electrical model and a thermal model. The electrical model was developed to simulate the resistive heat generation rate, $\dot{Q}$ (W/m^3), at the welding interface. This heat generation rate was then entered in the thermal model, which provided the welding temperature during the welding process.

3.1. Electrical model

An electrical model was developed to calculate the resistive heat generation rate, $\dot{Q}$, in the heating element as a function of the position of the connector wheels and the input power. The input power effectively used to generate heat at the heating element and the electrical properties of the heating element had to be determined as preliminary steps for the building of the electrical model.

3.1.1. Effective input power

Owing to internal and contact resistance in the electrical circuit of the welding setup, not all the power consumed during the welding process was effectively used to generate heat at the welding interface. The contact resistance between the mesh heating element and the block connectors was considered to be the major source of power not effectively used for heat generation at the welding interface in the CRW process. The internal resistance of the connector wheels and the block connectors as well as the contact resistance between them were neglected due to the low resistivity of copper and the smoothness of their contact surfaces.

Clamping force and contact resistance

As already known from literature, the clamping pressure applied between the connectors and the heating element plays a major role in the contact resistance [11]. In order to determine the relationship between clamping pressure and contact resistance in the CRW process, a separate experimental setup was built to measure the resistance of the heating element between two connector blocks under various clamping pressures (Figure 5). The experimental setup consisted of two 16 × 12.7 × 6 mm^3 block connectors located 27.4 mm apart in the middle of a 254 mm × 60 mm mesh sheet, as shown in Figure 5. The dimensions of the blocks and mesh as well as the distance between blocks were chosen to mimic the welding setup. A pneumatic cylinder was used to provide different levels of clamping pressure, ranging from 0.01 MPa to 4.8 MPa, between the connector blocks and the mesh. A 1.92 A DC current was applied between the block connectors. The voltage difference between the block connectors was measured using a TTi1906 multimeter and the corresponding electrical resistance was calculated using Ohm's law.

As shown in Figure 5, the electrical resistance between the two block connectors was found to decrease with increasing clamping pressure, as indicated in literature [11, 22]. The reduction in total resistance with increasing clamping pressure was attributed to more effective contact between the heating element and the electrical connectors. For clamping pressures below 0.2 MPa, relatively large deviations were observed in the resistance values. This could be the result of too small contact surface between the heating element and the electrical connectors. On the other hand, increasing the clamping pressure above 1 MPa showed no significant influence in the resistance values. Therefore the contact resistance was considered to be negligible at clamping pressures above 1 MPa.

Contact resistance in the CRW setup

The contact resistance in the actual CRW setup, R_c, was experimentally determined through the following steps:

i. The resistance of the welding circuit, $R_{total,}$ was calculated by dividing the total welding voltage by the current recorded during the welding process.

ii. The resistance of the mesh, $R_{mesh,}$ was measured using the experimental setup in Figure 5 for different positions of the connector blocks along the welding direction and a clamping pressure of 4 MPa, at which R_c was considered to be negligible.

iii. The contact resistance, R_c, was calculated as $R_c = R_{total} - R_{mesh}$

Three main observations could be drawn from the comparison between R_{total} and R_{mesh} for the whole welding process shown in Figure 6 (a):

i. Both R_{total} and R_{mesh} were higher towards the edges of the mesh, i.e. at the beginning and the end of the total welding area. The higher resistance values were attributed to changes in the electrical paths in the mesh heating element.

ii. Fluctuations were observed for the value of R_{total}. These fluctuations are attributed to variations in the contact between the block connectors and the mesh with the rolling of the copper wheels from one pair of block connectors to another, as sketched in Figure 6 (b). Since these fluctuations only occurred during relatively small time intervals, their effect on R_{total} was considered negligible.

iii. An average ratio between R_c and R_{mesh} of 0.25 was calculated from the data shown in Figure 6 (a). In order to do so, an average R_{total} value was calculated as a function of the X position of the connector wheels by curve fitting the experimental data in Figure 6 (a) with a suitable sixth-order polynomial. Likewise, R_{mesh} was defined as a function of the X position of the connector wheels through a sixth-order polynomial interpolation of the data points in Figure 6 (a). Subtracting these two functions for the different positions of the connector wheels allowed us to calculate an average R_c value.

Based on the ratio between R_C and R_{mesh} discussed above, a relationship between the input voltage, ΔU_{total}, and the actual voltage difference across the mesh heating element, ΔU_{mesh}, was defined as follows:

$$\Delta U_{mesh} = \frac{R_{mesh}}{R_{mesh} + R_c} \cdot \Delta U_{total} = 0.8 \cdot \Delta U_{total} \quad (1)$$

3.1.2. Electrical properties and modelling of the heating element

Due to the relatively complex geometry of the mesh heating element, modelling the exact mesh geometry was a difficult task. However, due to its relatively fine texture, the mesh heating element was modelled as a continuous medium, i.e. a conductive plate, with a certain equivalent resistivity and the same cross-sectional dimensions as the original heating element, 12 mm-wide x 0.08 mm-thick . A comparison between predicted and experimental results was conducted to validate this approach, as shown later in this section.

Equivalent resistivity of the mesh

The equivalent resistivity of the mesh heating element was determined by measuring the resistance of a mesh strip at various measurement lengths in the experimental setup depicted in Figure 7. In this setup a 12 mm-wide mesh strip and two 16 x 12.7 x 6 mm^3 block connectors were used. A clamping pressure of 4 MPa was applied between the connectors and the mesh. A constant 1.92 A DC current was applied between the connectors. The voltage difference between the connectors was measured using a TiT1906 multimeter and the resistance of the mesh was calculated using Ohm's law.

The results of these measurements are displayed in Figure 7. An equivalent resistivity for the mesh heating element amounting to ρ = 7.41e-6 Ω·m was calculated using curve fitting of the resistance measurements and the following formula for the resistivity of a continuous medium:

$$\rho = \frac{\Delta R}{\Delta L/(w \cdot h)} \tag{2}$$

where, L is the length of the mesh strip, w is the width of the conductive plate (w = 12mm), and h is the thickness of the conductive plate (h = 0.08 mm). ΔR, i.e. the resistance difference between two different lengths of heating element, was used in this calculation to rule out the effect of any potential contact resistance (although assumed to be negligible at 4 MPa clamping pressure).

It must be noted that he equivalent resistivity obtained for the heating element, 7.41e-6 Ω·m, was one order of magnitude higher than the electrical resistivity reported in literature for AISI 304L stainless steel, 7.2e-7 Ω·m [22]. This resulted from considering the heating element as a conductive plate with the same electrical resistance as the stainless steel mesh heating element. If the actual cross section of the mesh had been considered for calculating the electrical resistivity from the results presented in Figure 7, the experimental resistivity of the mesh would have amounted to 8.56e-7 Ω·m, assuming that only the wires that are connected to both connectors at the same time conduct the electricity and, hence, that the current flows in straight lines between the connectors . In that case, the value for the experimental resistivity of the mesh is similar but somewhat higher than the electrical resistivity of AISI 304L. This difference could be caused by the existence of some extra current flow paths additional to the ones considered to calculate the resistivity of the mesh.

Validation of mesh heating element as an equivalent conductive plate

In order to validate the approach of modelling the heating element as a continuous medium, i.e. a conductive plate, characterised by 7.41e-6 Ω·m equivalent resistivity and 12 mm-wide x 0.08 mm-thick cross section the experiment depicted in Figure 5 was modelled using COMSOL Multiphysics®.

Applying a constant current of 1.92 A to the electrical connectors, the voltage distribution in the mesh was predicted for various X-positions of the electrical connectors, see Figure 8 (a). Voltage differences, ΔU, across the stainless steel mesh in the actual experiment were measured using a voltmeter with wire probes in direct contact with the surface of the mesh and separated by 25.4 mm. A comparison of the voltage predicted by the model with the experimental measurements is shown in Figure 8 (b). As a result of the good agreement between the predicted and experimental results for ΔU, the approach of modelling the stainless steel mesh as a conductive plate was validated. Other observations drawn by the results in Figure 8 (b) are:

i. ΔU changes with the X position of the measurement points. A higher value of ΔU is obtained in the vicinity of the block connectors, implying that, as expected, the welding energy is mainly concentrated in the area between the two block connectors.
ii. ΔU is dependent on the X position of the block connectors. A higher ΔU, and hence a higher resistance of the welding electrical circuit, is obtained when the block connectors are located near the edges of the mesh. This result is in accordance with the results presented in Figure 6.

3.1.3. Resistive heat generation rate

A 3D COMSOL Multiphysics® electrical model (conductive media DC application mode) was created to predict the rate at which heat is generated at every location of the mesh heating element for every position of the copper wheel connectors. The model is based on the following equations:

$$\nabla \cdot \boldsymbol{J} = -\nabla \cdot \left(\frac{\nabla V}{\rho}\right) = 0 \tag{3}$$

$$\dot{Q} = \rho \boldsymbol{J}^2 \tag{4}$$

where **J** is the current density vector, V is the electric potential in the mesh heating element, ρ is the electrical resistivity, and $\dot{Q}$ is the rate at which resistive heating is generated by the mesh. It must be noted that, owing to the contact resistance, the electric potential at different locations in the mesh corresponded to an actual input voltage of 0.8 times the total input voltage, as indicated in Eq. 1.

Modelling the resistive heat generation rate, $\dot{Q}$, as a continuous function of the position in the mesh heating element was found to cause singularities around the corners of the block connectors (see Figure 9 (a)). Such singularities, which are believed to mainly result from geometrical discontinuities, were effectively smoothed by treating $\dot{Q}$ as a discrete function of the position in the mesh heating element. As shown in Figure 9 (b), the mesh heating element was hence discretized into a matrix consisting of 20

columns, or "welding areas", along the welding direction and 9 rows across the welding direction. Each welding area was delimited by one pair of opposite block connectors and hence all the columns had the same width. The height of the rows was however smaller in the vicinity of the block connectors to minimise the singularities in $\dot{Q}$ (see Figure 9 (b)). An average heat generation rate, $\dot{Q}_{ij,p}$, was calculated for each quadrant, being i the row number (from $i = 2\ to\ 8$), j the welding area in which heat generation is calculated and p the welding area were the connector wheels are positioned at a specific moment in the welding process (see Figure 9 (b)). The heat generated through contact resistance was taken into account as a constant heat generation rate equality distributed in rows 1 and 9, and expressed by:

$$\dot{Q}_c = \dot{Q}_{1j,p} = \dot{Q}_{9j,p} = \frac{(\Delta U_{total} - \Delta U_{mesh})^2}{R_c(V_{1j} + V_{9j})} = 0.16 \cdot \frac{\Delta U_{total}^2}{R_{mesh}(V_{1j} + V_{9j})} \qquad \text{if } j = p$$

$$\dot{Q}_c = \dot{Q}_{1j,p} = \dot{Q}_{9j,p} = 0 \qquad \text{if } j \neq p \tag{5}$$

where V_{ij} indicates the mesh volume enclosed in quadrant ij.

The effect of temperature on the resistance of the mesh heating element and hence on the resistive heating rate were not considered in this study due to the difficulties introduced by the use of average heat generation rates and by the resulting non-uniform temperature distributions. However, if the increasing resistance with temperature had been considered [21], the actual resistive heating rates might have been slightly lower.

As an example of the output of the electrical model, Figure 10 shows $\dot{Q}_{5j,p}$ for different positions of the connector wheels, $p = 1, 5, 10, 20$. As seen in this Figure, for a certain position of the connector wheels, resistive heat was mainly generated in between the two block connectors on which the connector wheels were located but also in the adjacent areas. It was also noticed that maximum $\dot{Q}$ was generated at $p =$ 1and $p = 20$, i.e. edges of the mesh heating element in the longitudinal direction. This is attributed to a higher current density at those locations due to a smaller effective area of mesh for the current to flow.

3.2. Thermal model

Once the heat generation rate was known as a function of time, i.e. location of the connector wheels, and as a function of the position in the mesh heating element, a 3D transient heat transfer model was developed using COMSOL Multiphysics®, with the exact geometry of the actual welding setup shown in Figure 3.

The material properties used by this model are summarized in Tables 1 and 2. The temperature-dependent specific heat of the GF/PPS laminates and the PPS film, shown in Table 2, were measured through differential scanning calorimetry (DSC) according to ASTME1269-11. The temperature-dependent thermal conductivity of the GF/PPS laminates was measured in the laboratories of Koninklijke DSM N.V., the Netherlands, using the laser flash method. The temperature dependent thermal conductivity of the PPS film was estimated using the rule of mixtures in Eq. 6.

$$k_m = \frac{(1 - V_f)k_c k_f}{k_f - V_f k_c} \tag{6}$$

The heat transfer model was based on the heat transfer equation:

$$\rho C_p \frac{\partial T}{\partial t} + \nabla \cdot (-k\nabla T) = \dot{Q} \tag{7}$$

where ρ is density, C_p is heat capacity, T is temperature, t is welding time, and k is thermal conductivity. The effect of the latent heat during melting of the polymer on the heat transfer problem was found to be negligible as in [12, 20, 26, 27], and therefore it was not taken into account in the model.

The boundary conditions were set as free convection and surface-ambient radiation, and described by the following equation:

$$-n \cdot (-k\nabla T) = h(T_{amb} - T) + \varepsilon\sigma(T_{amb}{}^4 - T^4) \tag{8}$$

where n is the normal vector of the boundary, h is the free convection coefficient to air ($h = 5\ \mathrm{W/m^2K}$) [28], T_{amb} is ambient temperature ($T_{amb} = 20$ °C), ε is surface emissivity ($\varepsilon = 0.95$) [28] and σ is the Stefan-Boltzmann constant ($\sigma = 5.67 \times 10^{-8}\ \mathrm{W/m^2K}$).

Concerning the heat transfer between the block connectors and the mesh heating element, the actual contact area between both elements was much smaller than the total clamping area due to the open gaps in the mesh and due to its woven nature, as sketched in Figure 11. Consequently, the model did not consider conductive heat transfer between the block connectors and the mesh heating element. Instead a more restrictive heat transfer scenario, described by a fixed heat flux from the mesh to the connectors (Eq. 9) with a heat flux coefficient $h = 5\mathrm{W/m^2K}$ [28], was considered between the heating element and the blocks connectors.

$$-n \cdot (-k\nabla T) = h(T_{amb} - T) \tag{9}$$

4. Results and discussion

4.1. Temperature distribution predicted by the model

A typical distribution of maximum welding temperatures at the welding interface as predicted by the process model is shown in Figure 12. Non-uniform temperature profiles were found both along and across the welding direction.

Along the welding direction, a relatively small temperature oscillation could be observed as shown in Figure 12. Higher temperatures could be found in the middle of each individual welding area (indicated by a red circle in Figure 12 right) than at the edges (indicated by black circles, Figure 12 right), which was attributed to faster heat transfer to the relatively colder adjacent material at the edges of each welding area. Moreover, and despite a higher resistive heat generation rate at $j = p = 1$ (see Figure 10), i.e. the first welding area at the beginning of the welding process, lower temperatures were observed there (see point A in Figure 12), caused by the absence of any previously welded areas and hence absence of preheating.

Across the welding direction, an "edge effect" was found consisting of a significant temperature difference between the edges and the middle of the overlap. Whereas the edge effect in RW processes usually entails lower temperatures at the edges of the overlap [21, 29], a higher edge temperature was found in the CRW process. The higher temperature at the edges of the overlap was attributed to a combination of the following factors: (i) heat radiated from the 1mm exposed heating element between the edge of the overlap and the block connectors, similar to what is observed at the ends of the weld in RW [29], (ii) concentration of resistive heating near the edges of the block connectors, and (iii) heat dissipation at the interface between the mesh and the block connectors as a result of the contact resistance.

4.2. Model validation

To validate the process model, the temperatures at the weld interface were measured experimentally. Eight K-type thermocouples, TC1-TC8, were placed between the neat resin layer and one of the adherends (see Figure 13). Thermocouples TC1, TC3, TC5, TC7 and TC8 were placed in the middle of welding areas 1, 3, 5, 7 and 8. Thermocouples TC2 and TC4 were placed at the edges of welding areas. TC6 was placed in the middle of welding area 6 but only 3 mm away from the edge of the overlap (see Figure 13).

A close agreement between predicted and measured temperature for two different welding speeds was obtained, as shown in Figure 14. It should be noted that the temperature measured by TC6 was above the prediction for both welding speeds, which could be a result of the discrete heat generation rates used in the model and/or inaccurate modelling of the contact resistance or the heat transfer between the heating

element and the block connectors, given the results in section 4.4 . It is also interesting to note how both predicted and measured temperatures showed clear steps in the cooling phase of the welding process, which are attributed to the superposition of the heat generated at different locations as the connecting wheels travel along the welding direction.

4.3. Sensitivity study on welding voltage and speed

Figure 15 shows the predicted effect of the input voltage and the welding speed in the welding temperature at the TC5 location, as defined in Figure 13. The welding temperature, i.e. the temperature at the middle of the overlap (e.g. TC5), was found to increase with decreasing welding speed (as also shown in Figure 14) and with increasing input voltage. The process model showed that a 100% increase in the input voltage (from 3 to 6V) yielded a 275% increase in the welding temperature (from 160 to 600°C). However, a 350% increase in the welding speed (from 0.28 to 1.27 mm/s) only yielded a 130% increase in the welding temperature (from 260 to 600°C). Based on these results, the welding temperature can be considered to be more sensitive to changes in the input voltage than changes in the welding speed.

Since both welding speed and input voltage influence the welding temperature, the selection of one parameter is also dependent on the selection of the other. As discussed above, a higher welding temperature can be obtained either by increasing the input voltage, or by decreasing the welding speed. Therefore different combinations of welding voltage and welding speed can be used to obtain the same predefined welding temperature, as shown in Figure 16.

Changing the welding voltage and/or the welding speed was found, however, not to have an effect on the ratio between the temperature at the edges and the temperature at the middle of the overlap (e.g. TC6/TC5), amounting to approximately 1.4. This results from the fact that voltage and speed are responsible for resistive heating, which governs heat generation both at the middle and at the edges of the welding overlap. Consequently, tuning of the welding voltage or welding speed changes the overall temperatures at the welding overlap but does not influence the relative size of the gap between temperature at the edges and at the middle of the overlap.

4.4. Effect of clamping pressure

The electrical clamping pressure directly influences the quality of the contact between block connectors and heating element. Consequently, it is directly related to the contact resistance between the mesh and the block connectors, as shown in section 3.1.1, and it is believed to also have an influence in the

efficiency of heat transfer between the heating element and the block connectors, as explained in section 3.2. Therefore the clamping pressure is suspected to have a major influence in the edge effect, which was further investigated using the process model.

Firstly, the effect of the contact resistance was investigated by using the process model to predict the distribution of welding temperatures across the overlap in (i) the actual welding setup, i.e. with a contact resistance amounting to 25% of the resistance of the mesh, and (ii) an ideal welding setup with zero contact resistance. A $h = 5\mathrm{W/m^2K}$ heat flux boundary condition at the mesh-block connector interface was assumed in both cases in order to isolate the effect of the contact resistance. The results, depicted in Figure 17 (a), show how the edge effect was indeed significantly decreased by considering zero contact resistance, while the welding temperatures in the middle of the overlap remained unchanged.

Secondly, the effect of heat transfer efficiency between the heating element and block connectors was investigated by predicting the temperature distribution across the overlap for a zero contact resistance setup in which the heat flux coefficient was increased from 5 W/m^2K to 100 W/m^2K and 500 W/m^2K . An ideal heat transfer scenario consisting of full conduction between the heating element and the block connectors was also considered in this analysis. The results, depicted in Figure 17 (b), show that the temperature at the edges of the overlap was significantly reduced when the heat transfer coefficient was increased from 5 to 500 W/m^2K and even further reduced when full conduction between the heating element and the block connectors was assumed.

4.5. Effect of the size of the block connectors

The width of the block connectors is directly related to the size of the melt zone (see Figure 1) and it is, therefore, expected to have an effect on the welding process. In order to further investigate this potential effect, the relationship between block width and resistance of the welding electrical circuit was firstly analysed by modelling the experimental setup shown in Figure 5. The results of this simulation, shown in Figure 18 (a), indicated that the resistance of the welding electrical circuit created between each pair of electrified block connectors decreases with increasing width of the connectors. This results from the fact that increasing the width of the block connector is analogous to increasing the effective cross section of the mesh heating element.

Secondly, the relationship between the width of the block connectors and the welding temperature was analysed by using the CRW process model. The welding temperature at TC5 was simulated using a fixed welding voltage of 4.3 V and a fixed welding speed of 0.85 mm/s. Zero contact resistance was considered

in this simplified analysis. As shown in Figure 18 (a), the welding temperature was found to increase with increasing width of the block connectors. Therefore, increasing the width of the block connectors allows higher welding speeds for a fixed welding temperature, as seen in Figure 18 (b). However, due to the increased resistance, the faster welding speeds come at the cost of increased input power. Consequently, the maximum capacity of the power supply must be taken into account when determining the width of the block connectors.

5. Conclusions

A three-dimensional finite element process model was developed to simulate continuous resistance welding of thermoplastic composites. The continuous welding process modelled in this study was characterised by the use of a single-piece stainless steel woven mesh as the heating element and multiple adjacent copper block connectors along the welding direction. The process model consisted of an electrical model, used to predict heat generation at the mesh heating element, and a thermal model, used to simulate the temperatures reached during welding. In order to validate the process model, temperature was measured at different locations in the welding interface during continuous resistance welding of glass fibre reinforced polyphenylene sulfide laminates in a single-overlap configuration. Subsequently, the effects of electrical clamping pressure, welding voltage, welding speed and size of the block connectors on the welding process were investigated using the process model. The main conclusions drawn from this study are:

- The welding temperatures predicted by the process model were in good agreement with the temperatures measured both along and transverse to the welding direction. The temperature distribution along the welding direction was found to be fairly uniform. Contrarily, significant non-uniformities were observed in the temperature distribution transverse to the welding direction, in particular, the temperature was found to be substantially higher towards the edges than in the middle of the overlap.
- Both the contact resistance and the efficiency of heat transfer between the heating element and the block connectors, which are believed to be directly related to the clamping pressure applied on the block connectors, were found to have a large influence on the temperature distribution transverse to the welding direction. Decreasing the contact resistance and increasing the effectiveness of heat transfer between the heating element and the block connectors, which are

believed to happen when the clamping pressure is increased, was shown by the process model to be an effective way to reduce the higher welding temperature observed near the edges of the overlap.

- Welding voltage and welding speed were found to be the two most influential parameters for the welding temperature. A higher welding temperature could be obtained by either increasing the welding voltage or decreasing the welding speed. The welding temperature was found to be more sensitive to the welding voltage than to the welding speed.
- The size of the block connectors was found to influence the selection of the welding parameters. A higher welding speed can be achieved if wider block connectors are used, however, this comes at a cost as more input power is required for the welding process.

Acknowledgements

The authors would like to express their gratitude for the support provided by TenCate Advanced Composites, The Netherlands. H. Shi thanks the PhD Scholarship Fund from China Scholarship Council (CSC) for overseas study.

References

[1] Stavrov D, Bersee HEN. Experimental investigation of resistance welding of thermoplastic composites with metal mesh heating element. SAMPE-Europe conference proceedings. Paris, France2004.

[2] Chang IY, Lees JK. Recent Development in Thermoplastic Composites: A Review of Matrix Systems and Processing Methods. Journal of Thermoplastic Composite Materials. 1988;1(3):277-96.

[3] Offringa A, Myers D, Buitenhuis A. Redesigned A340-500/600 Fixed Wing Leading Edge (J-Nose) in Thermoplastics. Proceedings of the 22nd International SAMPE Europe conference. Paris, France2001. p. 331-43.

[4] Ingen JWv, Buitenhuis A, Wijngaarden Mv, III FS. Development of the Gulfstream G650 induction welded thermoplastic elevators and rudder. SAMPE International Conference 2010. Seattle, U.S.A2010.

[5] Stavrov D, Bersee HEN. Resistance welding of thermoplastic composites-an overview. Composites Part A: Applied Science and Manufacturing. 2005;36(1):39-54.

[6] Yousefpour A, Hojjati M, Immarigeon J-P. Fusion Bonding/Welding of Thermoplastic Composites. Journal of Thermoplastic Composite Materials. 2004;17(4):303-41.

[7] Ageorges C, Ye L, Hou M. Advances in fusion bonding techniques for joining thermoplastic matrix composites: a review. Composites Part A: Applied Science and Manufacturing. 2001;32(6):839-57.

[8] Hou M, Yang M, Beehag A, Mai Y-W, Ye L. Resistance welding of carbon fibre reinforced thermoplastic composite using alternative heating element. Composite Structures. 1999;47(1-4):667-72.

[9] Stavrov D, Bersee HEN, Beukers A. Resistance Welding of Continuous Fibre Reinforced PPS Composites with Metal Mesh Heating Element. 1st International Conference on Innovation and Integration in Aerospace Sciences. Queen's University Belfast, Northern Ireland, UK.2005.

[10] Dubé M, Hubert P, Yousefpour A, Denault J. Resistance welding of thermoplastic composites skin/stringer joints. Composites Part A: Applied Science and Manufacturing. 2007;38(12):2541-52.

[11] Ageorges C, Ye L, Hou M. Experimental investigation of the resistance welding for thermoplastic-matrix composites. Part I: heating element and heat transfer. Composites Science and Technology. 2000;60(7):1027-39.

[12] Talbot É, Hubert P, Dubé M, Yousefpour A. Optimization of thermoplastic composites resistance welding parameters based on transient heat transfer finite element modeling. Journal of Thermoplastic Composite Materials. 2013;26(5):699-717.

[13] Lambing CLT, Don RC, Andersen SM, Holmes ST, Leach BS, Gillespie JW. Design and Manufacture of an Automated Resistance Welder for Thermoplastic Composites. 49th Annual Technical Conference (ANTEC '90)1991. p. 2527-31.

[14] McKnight SH, Holmes ST, Gillespie JW, Lambing CLT, Marinelli JM. Scaling issues in resistance-welded thermoplastic composite joints. Advances in Polymer Technology. 1997;16(4):279-95.

[15] Yousefpour A, Octeau M-A. Resistance Welding of Thermoplastics. US20090032184 A1. Canada2009.

[16] Ageorges C, Ye L, Mai Y-W, Hou M. Characteristics of resistance welding of lap-shear coupons. Part III. Crystallinity. Composites Part A: Applied Science and Manufacturing. 1998;29(8):921-32.

[17] Ageorges C, Ye L, Mai Y-W, Hou M. Characteristics of resistance welding of lap shear coupons.: Part II. Consolidation. Composites Part A: Applied Science and Manufacturing. 1998;29(8):911-9.

[18] Colak ZS, Sonmez FO, Kalenderoglu V. Process Modeling and Optimization of Resistance Welding for Thermoplastic Composites. Journal of Composite Materials. 2002;36(6):721-44.

[19] Maffezzoli AM, Kenny JM, Nicolais L. Welding of PEEK/carbon fiber composite laminates. SAMPE Journal. 1989;25(1):35-40.

[20] Jakobsen TB, Don RC, Gillespie JW. Two-Dimensional thermal analysis of resistance welded thermoplastic composites. Polymer Engineering & Science. 1989;29(23):1722-9.

[21] Shi H, Villegas IF, Bersee HEN. Modelling of Heat Transfer and Consolidation For Thermoplastic Composites Resistance Welding. 18th International Conference on Composites Materials. Jeju, South Korea2011.

[22] Stavrov D, Bersee HEN, Beukers A. The Influence of the heating element on resistance welding of thermoplastic composite materials. ICCM-14 Conference. 2003.

[23] http://k-mac-plastics.net/data%20sheets/gpo3_technical_data.htm. GP03 Technical Data. K-mac Plastics. 2012.

[24] http://www.tencate.com. CETEX® PPS Technical Data. TenCate2009.

[25] http://www.chrtape.com/cloth-glass-tape.aspx. CHR® Cloth-Glass Tape. Saint-Gobain. 2011.

[26] Xiao XR, Hoa SV, Street KN. Processing and Modelling of Resistance Welding of APC-2 Composite. Journal of Composite Materials. 1992;26(7):1031-49.

[27] Ageorges C, Ye L, Mai Y-W, Hou M. Characteristics of resistance welding of lap shear coupons. Part I: Heat transfer. Composites Part A: Applied Science and Manufacturing. 1998;29(8):899-909.

[28] Holmes ST, Gillespie JW. Thermal Analysis for Resistance Welding of Large-Scale Thermoplastic Composite Joints. Journal of Reinforced Plastics and Composites. 1993;12(6):723-36.

[29] Talbot E, Yousefpour A, Hubert P, Hojjati M. Thermal Behavior During Thermoplastic Composites Resistance Welding Annual Conference of The Society of Plastics Engineers (ANTEC) 2005 Boston, Massachusetts2005.

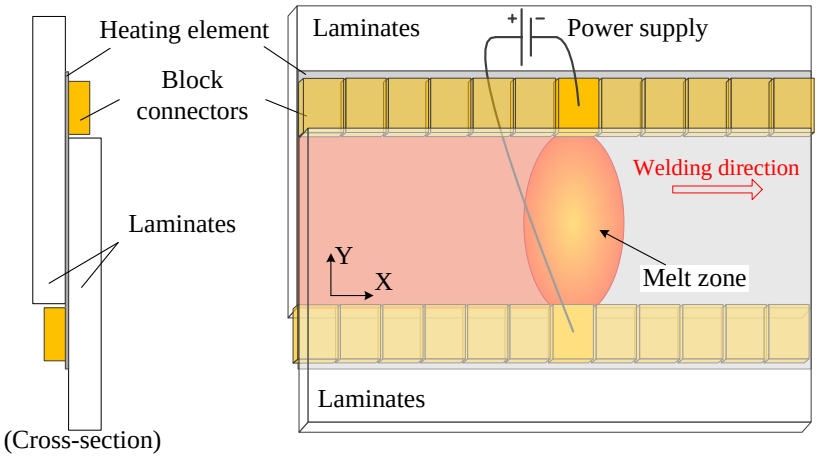

Figure1. A schematic diagram of continuous resistance welding of single-lap joints.

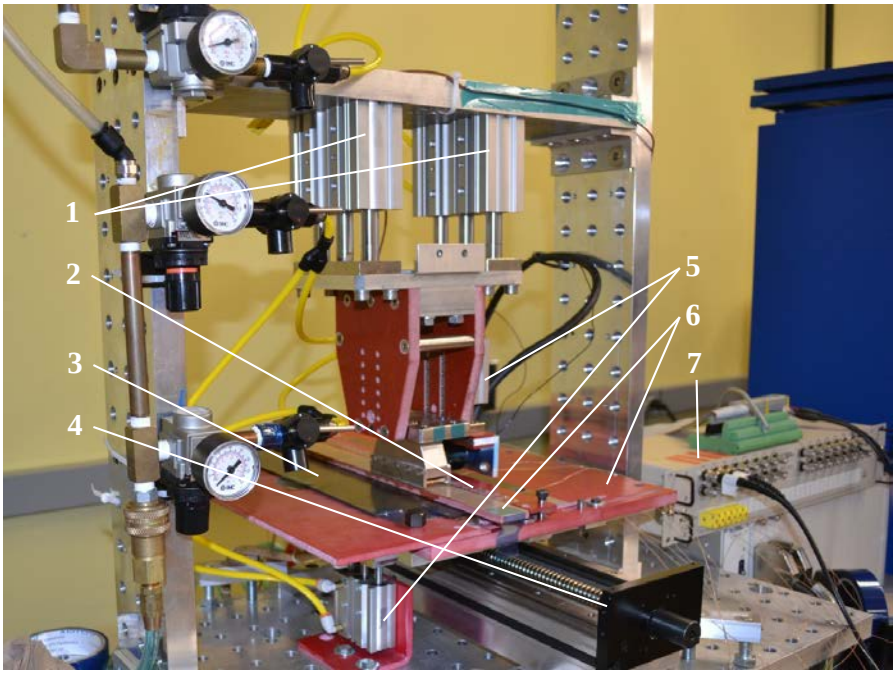

Figure 2. Continuous resistance welding setup, consisting of 1) pneumatic system for welding compaction, 2) block connectors, 3) laminates, 4) motion system, 5) pneumatic system for clamping, 6) insulators, and 7) power supply.

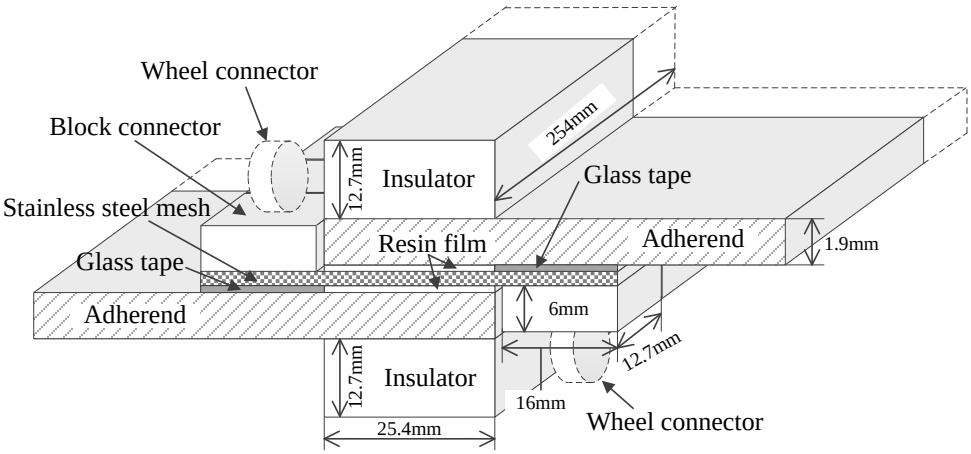

Figure 3. Geometry of continuous welding setup for the welding of single lap shear joint

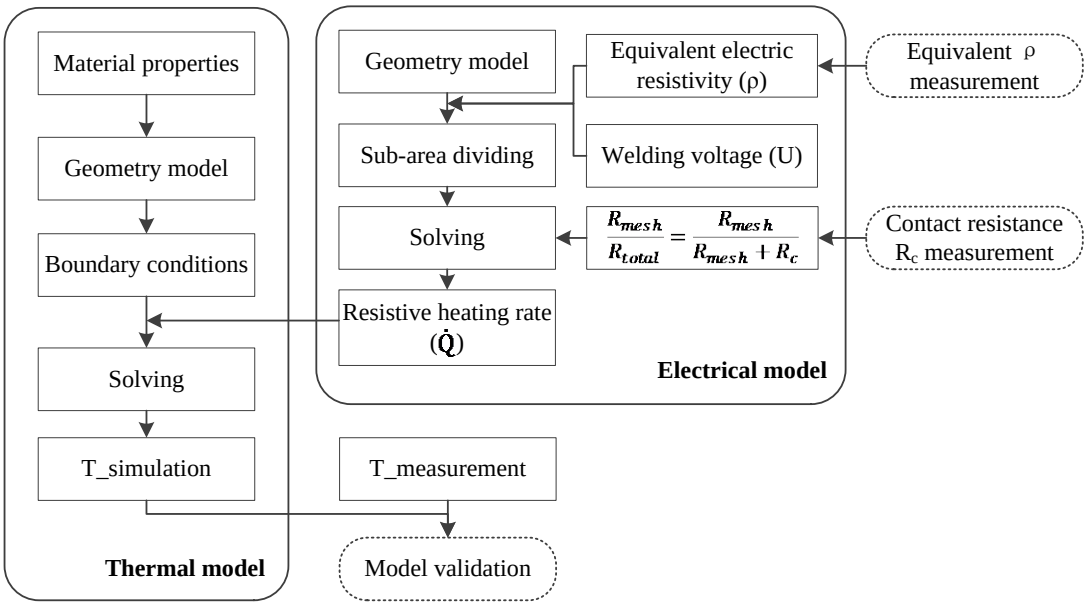

Figure 4. A flowchart of the process modelling for CRW.

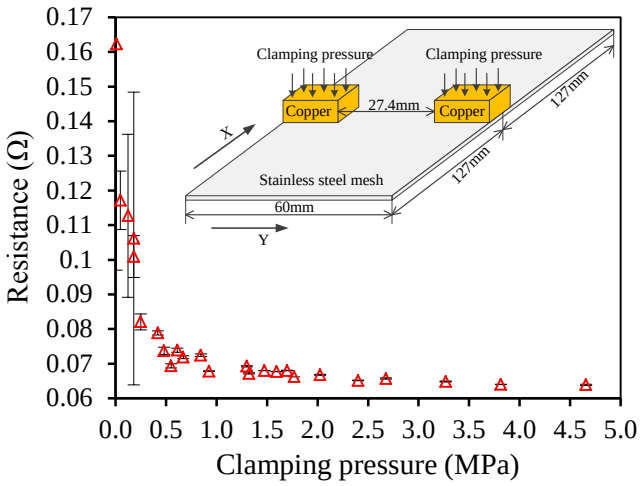

Figure 5. Resistance of the mesh versus clamping pressure.

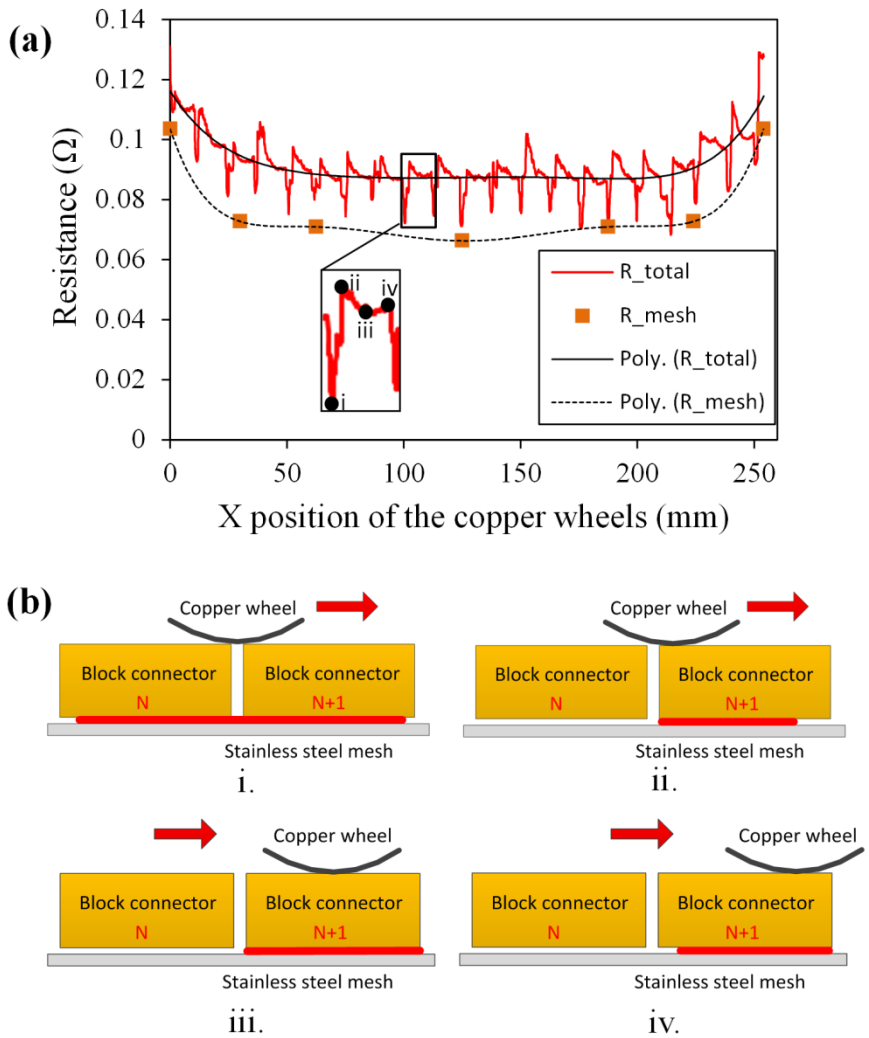

Figure 6. (a) Total resistance versus mesh resistance for an actual welding process. (b) Influence of location of connector wheels and contact between mesh and block connectors.

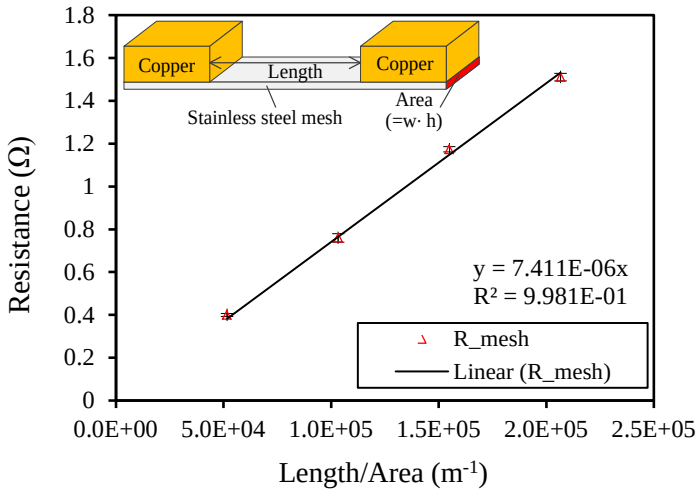

Figure 7. Experimental relationship between the resistance and the length of the mesh heating element.

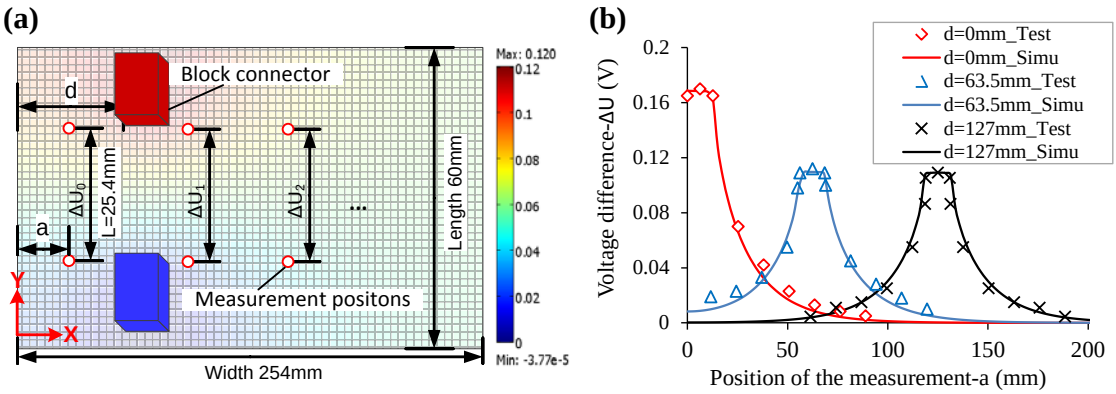

Figure 8. (a) Predicted voltage distribution in the heating element (b) Predicted and experimental voltage difference distribution for three different positions of the electrified block connectors.

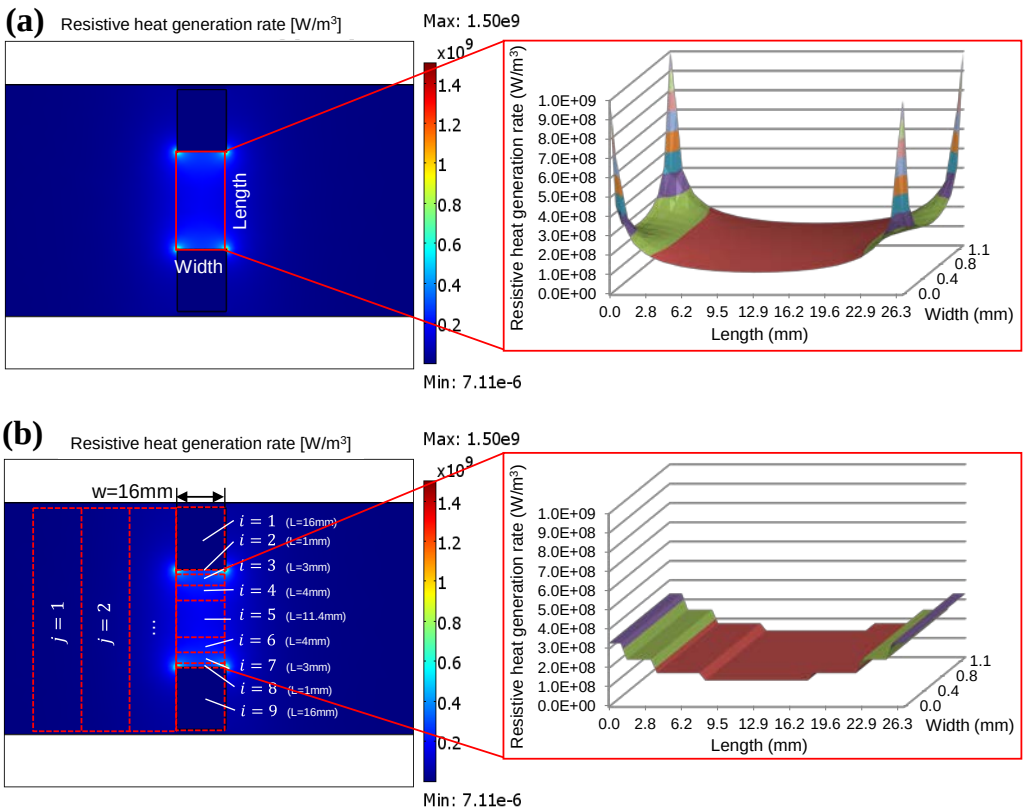

Figure 9. (a) Predicted $\dot{Q}$ distribution as a continuous function of the position in the mesh (1 V welding voltage). (b) Predicted $\dot{Q}$ distribution as a discrete function of the position in the mesh (1 V welding voltage).

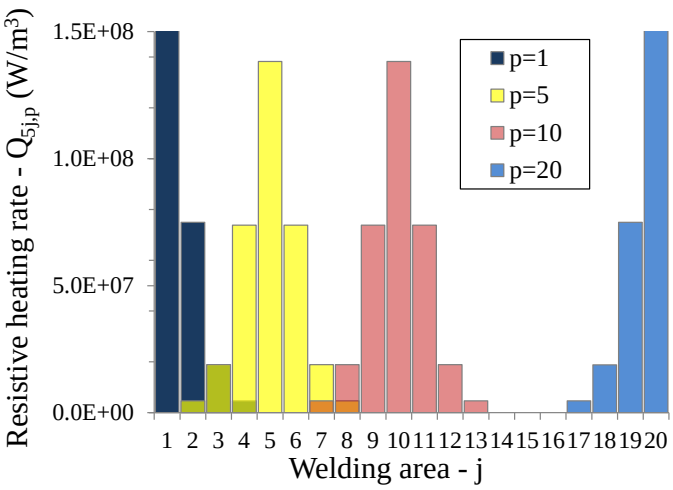

Figure 10. Average resistive heating rate in central row, i = 5, for different positions of the wheel connectors, p = 1, 5, 10, 20 under a 1 V constant voltage

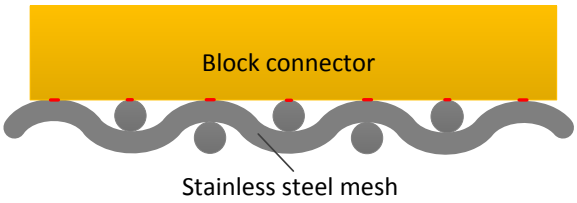

Figure 11. Schematic diagram of contact interface between the stainless steel mesh and the block connectors.

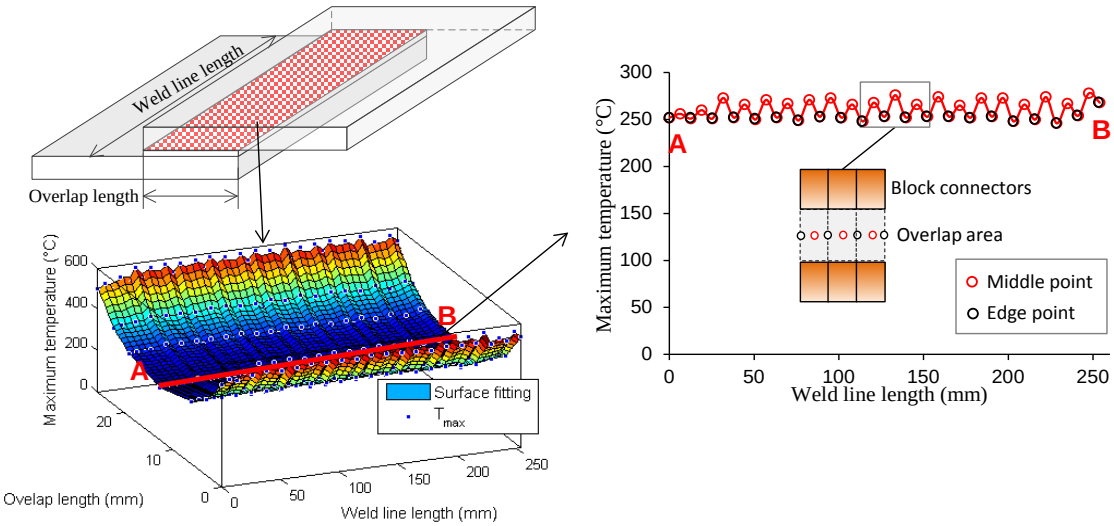

Figure 12. Predicted distribution of welding temperatures at the welding interface along and across the welding direction for 4.3 V constant welding voltage, 1.27 mm/s welding speed and 0.3 MPa electrical clamping pressure.

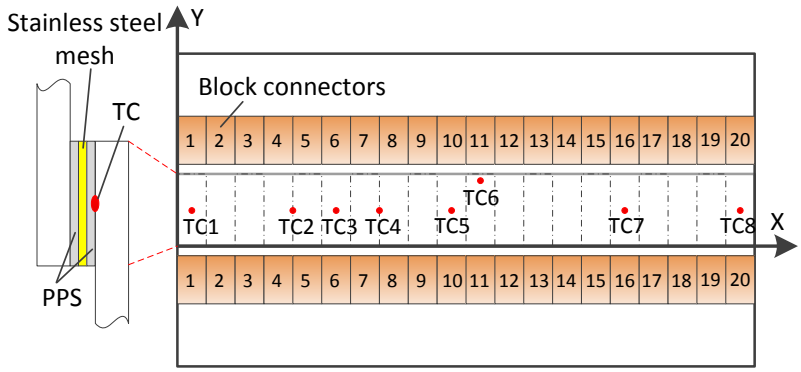

Figure 13. Positions of the thermocouples used for temperature measurement.

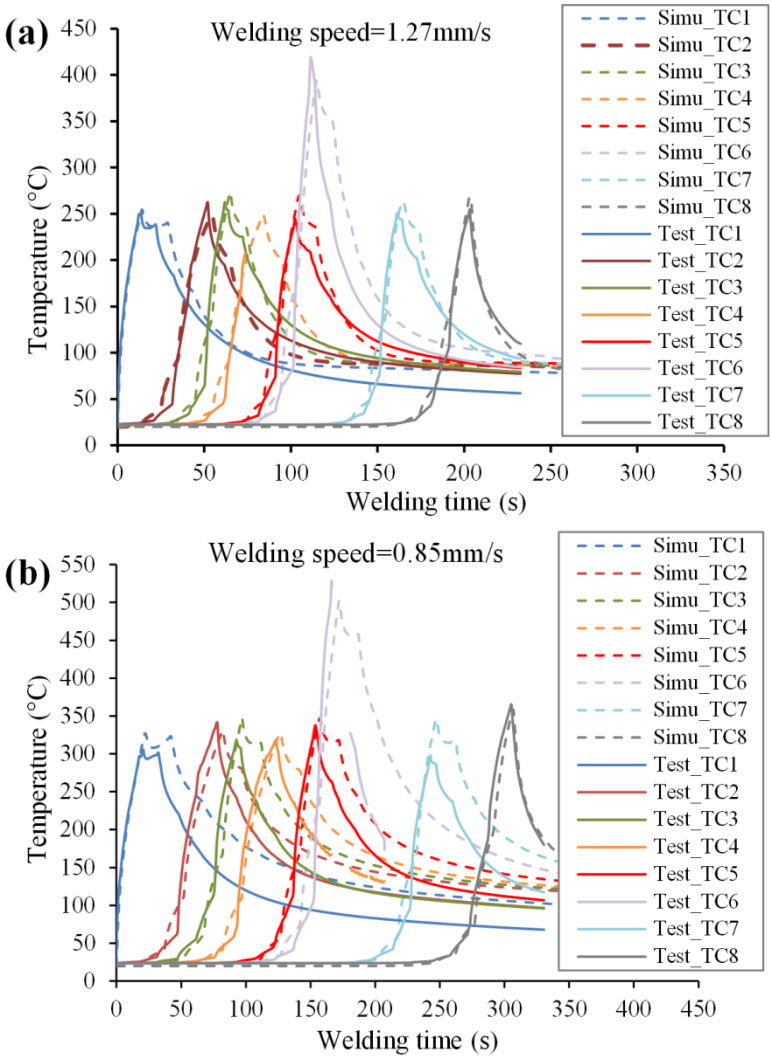

Figure 14. Comparison between predicted and measured temperature evolution at different locations in the welding interface for 4.3 V welding voltage and (a) 1.27 mm/s and (b) 0.85 mm/s welding speed.

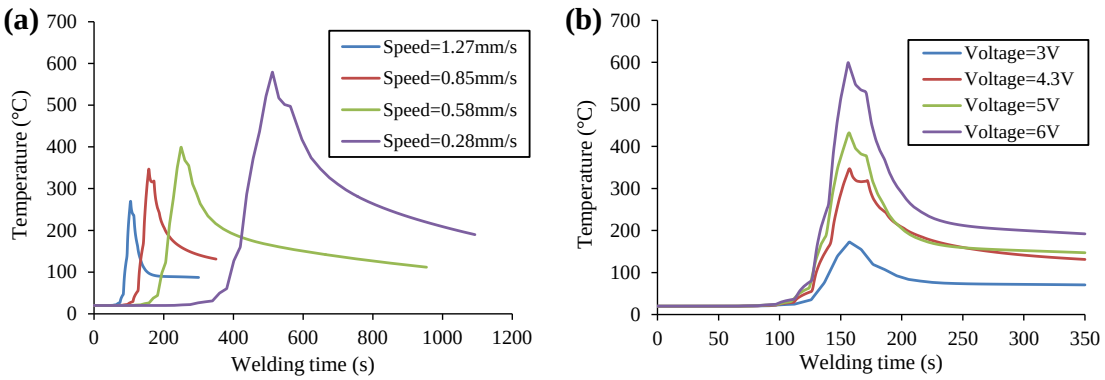

Figure 15. (a) Influence of welding speed on welding temperature at TC5 for 4.3 V welding voltage; and (b) influence of welding voltage on welding temperature at TC5 for 0.85 mm/s welding speed.

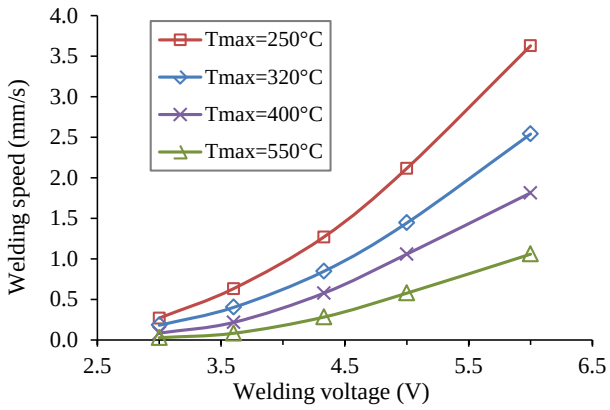

Figure 16. Welding speed and input voltage combinations for different maximum welding temperatures at TC5 location.

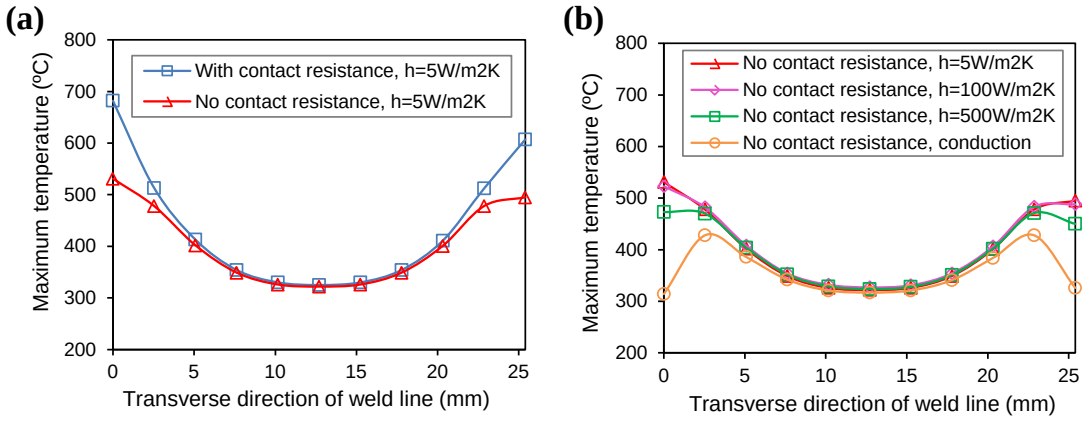

Figure 17. Temperature distribution across the weld direction atwelding area 10; (a) effect of contact resistance (for a fixed heat transfer scenario) and (b) effect of increased heat transfer efficiency represented by increased heat flux, h, and ending in ideal full conduction between the heating element and the block connectors .

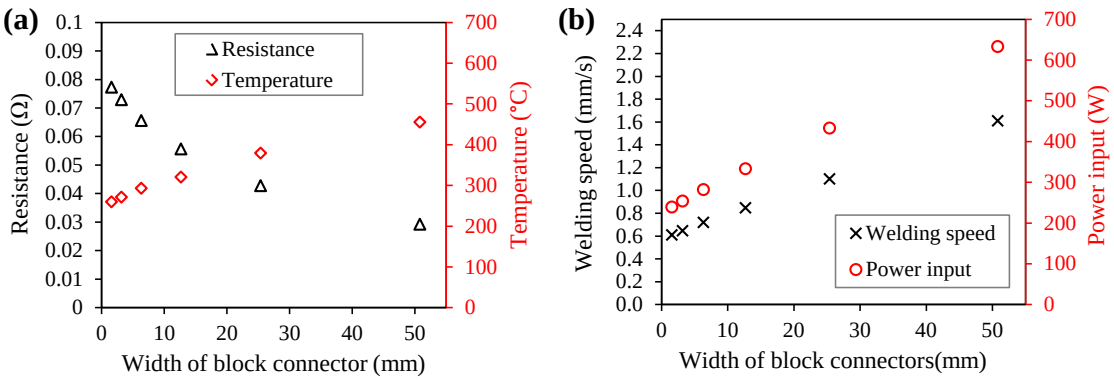

Figure 18. Effect of the width of block connectors on (a) resistance of the welding electrical circuit between two electrified block connectors and welding temperature (4.3 V and 0.85 mm/s welding voltage and speed, respectively); (b) selection of welding speed and required power input for the welding process (320 °C welding temperature and 4.3 V welding voltage).

Table 1. Room temperature material properties

	Density	Specific heat	Thermal conductivity		Reference
	ρ (kg/m^3)	C_p (J/kg·°C)	k_{xx}, k_{yy} (W/m·°C)	k_{zz} (W/m·°C)	
Stainless steel mesh	7780	460	10	10	[21]
GPO3 Fibre glass sheet	1795.5	1150	3.3	3.3	[23]
PPS resin film	1350	1090	0.19	0.19	[24]
GF/PPS	1900	900	0.53	0.42	ρ: [24] C_p, k: Measured
Glass tape	2079	1073	1.4	1.4	[25]

Table 2. Temperature-dependent properties of GF/PPS and PPS

Temp (°C)	GF/PPS			PPS	
	Specific heat	Thermal conductivity		Specific heat	Thermal conductivity
	C_p	k_{xx}, k_{yy}	k_{zz}	C_p	k
	(J/kg·°C)	(W/m·°C)	(W/m·°C)	(J/kg·°C)	(W/m·°C)
20	900	0.53	0.42	1090	0.19[b]
70	1030	0.57	0.44	1250	0.265[b]
120	1160	0.59	0.45	1510	0.272[b]
170	1250	0.61	0.45	1690	0.272[b]
220	1390	0.64	0.46	1970	0.279[b]
270	1380	0.62	0.38	1950	0.22[b]
320	1488	0.62[a]	0.38[a]	2166	0.22[b]

[a] Linearly extrapolated value

[b] Estimated using the rule of mixtures